Quark-mass effects in gradient-flow observables through next-to-next-to-leading order in QCD

R.V. Harlander and R.H. Mason

TTK, RWTH Aachen University, Sommerfeldstr. 16, 52074 Aachen, Germany

Abstract

We provide results for the vacuum expectation values of the flowed action density, the quark condensate, and the quark kinetic operator in the gradient-flow formalism. We work in $N_{\rm F}$-flavor QCD, keeping the heaviest quark massive and all others massless. The vacuum expectation values of these operators are calculated numerically through next-to-next-to-leading order QCD, providing important input for the extraction of fundamental QCD parameters from lattice calculations. While the focus is on charm- and bottom-quark mass effects, we provide the results in a form that is independent of the specific quark mass.

Contents

1 Introduction

The gradient-flow formalism (GFF) [1–5] is a method to exponentially suppress the high-momentum modes of fields in a symmetry-preserving way. This suppression is governed by the flow time t, which is a parameter of mass dimension two. Flowed fields are then defined to exist in the five-dimensional space $(x, t \geq 0)$, such that they regain their interpretation as physical fields on the boundary at $t = 0$. At $t > 0$, they are determined by the flow equations, which are differential equations of first-order in t.

The GFF was first developed for use in lattice field theory and has since seen much utility on the lattice, predominantly for the purpose of scale-setting [3, 6, 7]. While on the lattice, the flow equations are solved numerically, the gradient flow can also be approached perturbatively [4, 5]. In fact, in some applications, the combination of lattice and perturbative results is crucial within the GFF. For example, the short-flow-time expansion (SFTX) allows one to relate flowed and regular operators via perturbative matching coefficients. This circumvents the conventional operator renormalization on the lattice and thus avoids operator mixing when taking the continuum limit. In a sense, the GFF offers a renormalization scheme which is both accessible on the lattice and in perturbation theory. Examples for practical applications are the computation of meson lifetimes [8, 9], the energy-momentum tensor [10, 11], and moments of parton-density functions [12, 13].

The main motivation for the current paper, on the other hand, is the determination of the strong coupling (or, equivalently, the QCD scale Λ_{QCD}) and the quark masses. Being fundamental parameters of QCD, any uncertainty in their value directly feeds into the computation of many processes and consequently much importance must be attached to quantifying them as precisely as possible. Currently, there are numerous efforts devoted to computing these quantities (for reviews, see Refs. [7, 14]), some of them based on the GFF (see, e.g., Refs. [15–21]). The vacuum expectation values (VEVs) of certain quark bilinear operators and the gluonic action density play a crucial role in many of these

methods. In a suitable renormalization scheme, these are renormalization group (RG) invariant quantities and can be computed both on the lattice and in perturbation theory. Comparison of the two thus provides a link between the hadronic phase of QCD and its fundamental Lagrangian parameters.

The accuracy of such extractions is determined by both the uncertainty of the lattice and the perturbative calculation, of course. As a general rule, in a perturbative QCD calculation, the residual dependence of a fixed-order result on the renormalization scale μ is used as an estimate of the theoretical uncertainty of that result. At leading order (LO), the μ-dependence is typically monotonous, making it difficult to choose a particular interval for the scale variation. Since the quark bilinear operators are independent of the strong coupling, the scale variation even vanishes at LO if the VEVs are expressed in terms of on-shell quark masses, while at next-to-leading order (NLO), it is monotonous [20]. In the case of the action density, the quark-mass dependence of its VEV occurs only at NLO, while from the massless calculation we know that next-to-next-to-leading order (NNLO) effects are quite crucial for a precise perturbative prediction. These observations motivate a calculation of the quark-mass effects for the corresponding VEVs to NNLO, which is the purpose of this paper.

Its remaining structure is as follows. In Section 2 we cover the basics of the GFF within perturbation theory. Section 3 defines the observables under consideration and their renormalization; it also briefly discusses the methods we employ to compute them through NNLO QCD. In Section 4 we provide numerical results in a form that is independent of the specific quark mass. These results are also provided in computer-readable format in an ancillary file accompanying this paper. Section 5 then studies the mass effects in the context of physical parameters, and Section 6 contains our conclusions.

2   Flow equations

Working in Euclidean space, we write the quantized regular QCD Lagrangian as

$$\mathcal{L}_{\mathrm{QCD}} = \frac{1}{4g_0^2} F_{\mu\nu}^a F_{\mu\nu}^a + \sum_{f=1}^{N_{\mathrm{F}}} \bar{\psi}_f \left(\slashed{D}^F + m_{f,0} \right) \psi_f + \mathcal{L}_{\mathrm{gf}} + \mathcal{L}_{\mathrm{gh}} \,, \tag{1}$$

with the gauge-fixing and ghost terms

$$\mathcal{L}_{\mathrm{gf}} = \frac{1}{2\xi_0} \left(\partial_\mu A_\mu^a \right)^2 \,, \qquad \mathcal{L}_{\mathrm{gh}} = \partial_\mu \bar{c}^a D_\mu^{ab} c^b \,, \tag{2}$$

respectively. Here, A_μ^a is the gluon field with color index a, ψ_f is the Dirac spinor for a quark of flavor f and bare mass $m_{f,0}$, c and $\bar{c}$ are the ghost and anti-ghost fields,

respectively, ξ_0 is the bare gauge parameter, and g_0 the bare gauge coupling. The field strength tensor is defined as

$$F_{\mu\nu}^a = \partial_\mu A_\nu^a - \partial_\nu A_\mu^a + f^{abc} A_\mu^b A_\nu^c \,, \tag{3}$$

with the SU(3) structure constants f^{abc}, and the covariant derivative in the fundamental representation is

$$D_\mu^F = \partial_\mu + A_\mu^a \frac{\lambda^a}{2} \,, \tag{4}$$

with λ^a the Gell-Mann matrices.

The GFF can be defined by adding the following two terms to the regular QCD Lagrangian:

$$\mathcal{L}_{\mathrm{QCD}}^{\mathrm{flow}} = \mathcal{L}_{\mathrm{QCD}} + \mathcal{L}_B + \mathcal{L}_\chi \,, \tag{5}$$

with

$$\mathcal{L}_B = \int_0^\infty \mathrm{d}t \, L_\mu^a \mathcal{F}_\mu^a \,, \qquad\qquad \mathcal{L}_\chi = \sum_{f=1}^{N_{\mathrm{F}}} \int_0^\infty \mathrm{d}t \left[\bar{\lambda}_f \mathcal{F}_\chi^f + \bar{\mathcal{F}}_\chi^f \lambda_f \right] \,,$$

$$\mathcal{F}_{B,\mu}^a = \partial_t B_\mu^a - \mathcal{D}_\nu^{ab} G_{\nu\mu}^b - \kappa \mathcal{D}_\mu^{ab} \partial_\nu B_\nu^b \,, \qquad \mathcal{F}_\chi^f = \left(\partial_t - \Delta - \kappa \, \partial_\nu B_\nu^b \right) \chi_f \,, \tag{6}$$

$$\bar{\mathcal{F}}_\chi^f = \bar{\chi}_f \left(\overleftarrow{\partial}_t - \overleftarrow{\Delta} - \kappa \, \partial_\nu B_\nu^b \right) \,.$$

The flowed covariant derivative in the adjoint representation is defined as

$$\mathcal{D}_\mu^{ab} \;\; = \;\; \delta^{ab} \partial_\mu - f^{abc} B_\mu^c \,, \tag{7}$$

and Δ and $\overleftarrow{\Delta}$ are the flowed covariant d'Alembert operator and its left-acting counterpart, defined according to

$$\Delta = \mathcal{D}_\mu^F \mathcal{D}_\mu^F \,, \qquad\qquad \overleftarrow{\Delta} = \overleftarrow{\mathcal{D}}_\mu^F \overleftarrow{\mathcal{D}}_\mu^F \,,$$

$$\mathcal{D}_\mu^F = \partial_\mu + B_\mu^a \frac{\lambda^a}{2} \,, \qquad \overleftarrow{\mathcal{D}}_\mu^F = \overleftarrow{\partial}_\mu - B_\mu^a \frac{\lambda^a}{2} \,, \tag{8}$$

The flowed field strength tensor $G_{\mu\nu}^a$ is related to Eq. (3) by replacing A_μ^a by B_μ^a.

The Euler-Lagrange equations for the Lagrange multiplier fields L_μ^a, λ_f, and $\bar{\lambda}_f$ yield the actual flow equations for the flowed gluon field B_μ^a and the flowed quark fields χ_f and $\bar{\chi}_f$:

$$\mathcal{F}_{B,\mu}^a = 0 \,, \qquad \mathcal{F}_\chi^f = 0 \,, \qquad \bar{\mathcal{F}}_\chi^f = 0 \,. \tag{9}$$

The flowed fields thus depend on the flow-time t which is a new parameter with mass dimension $= -2$. In Eq. (6), κ is an unphysical gauge parameter associated with the gradient flow and is generally taken to unity.
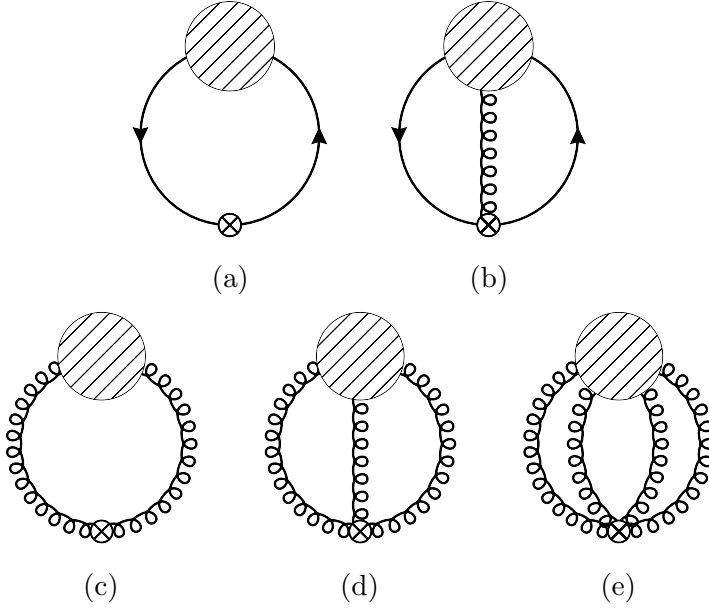
4

Figure 1: Diagrams contributing to the vacuum expectation value of the quark condensate $S_f(t)$ (a), the quark kinetic operator $R_f(t)$ (a/b), and the gluon condensate $E(t)$ (c–e). The hatched bubble represents an arbitrary flowed-QCD sub-diagram. Some of the lines can also be flowlines. All Feynman diagrams in this paper were created with `FeynGame` [23–25].

In addition to Eq. (9), one imposes the "initial conditions"

$$B_\mu(t=0,x) = A_\mu(x), \qquad \chi_f(t=0,x) = \psi_f(x), \qquad \bar{\chi}_f(t=0,x) = \bar{\psi}_f(x). \tag{10}$$

Eqs. (5) and (10) can be translated into Feynman rules involving simple generalizations of the regular quark and gluon propagators, as well as a gluon and a quark *flowline*, induced by the mixing with their respective Lagrange multiplier fields. As opposed to the propagators, the flowline does not involve a momentum pole. Furthermore, in addition to the regular QCD vertices, the flow terms of Eq. (6) induce a number of vertices between flowed fields and their Lagrange multiplier fields. The complete set of Feynman rules for flowed QCD can be found in Ref. [22].
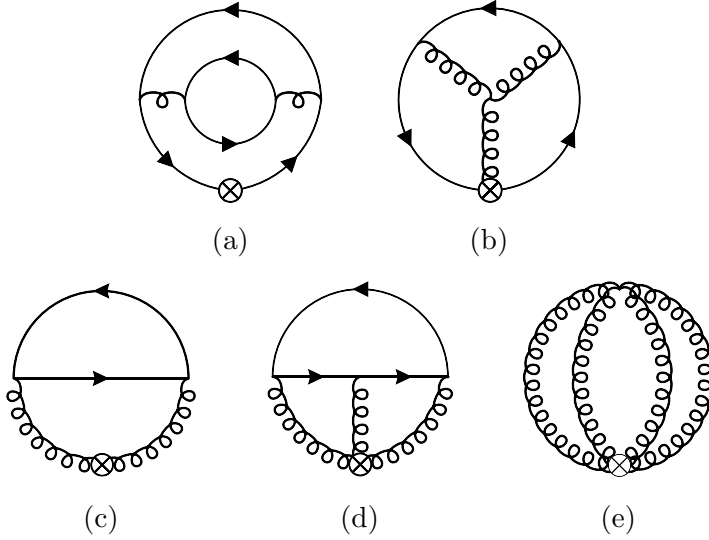
Figure 2: Specific diagrams contributing to $S(t)$ (a), $R(t)$ (a/b) at the three-loop level and $E(t)$ at the two- (c) and three-loop level (d) and (e).

3   Vacuum expectation values

3.1   Definitions

For the purposes of this study we will consider the mass effects on the VEVs of three operators: the quark condensate $S_f(t)$, the quark kinetic density $R_f(t)$, and the action density $E(t)$. These are described by

$$
\begin{aligned}
S_f(t) &= \langle \bar{\chi}_f(t)\chi_f(t)\rangle, \\
R_f(t) &= \langle \bar{\chi}_f(t) \overset{\leftrightarrow}{\slashed{\mathcal{D}}} \chi_f(t)\rangle, \\
E(t) &= \frac{1}{4}\langle G^a_{\mu\nu}(t)G^{a,\mu\nu}(t)\rangle,
\end{aligned}
\tag{11}
$$

where $\overset{\leftrightarrow}{\mathcal{D}_\mu} = \mathcal{D}^F_\mu - \overset{\leftarrow}{\mathcal{D}}^F_\mu$. Diagrammatically, these are represented by vacuum diagrams with an operator insertion. Fig. 1 displays the general form of diagrams for each of these processes, with Fig. 2 providing specific examples in each case.

The quark condensate $S_f(t)$ vanishes in the massless-quark case due to chiral symmetry. For an arbitrary quark mass, it was first calculated at one-loop level in Refs. [5, 26], and to two loops in Ref. [27]. Keeping only the leading (linear) term in the quark masses, the

6

three-loop result was obtained in Ref. [22]. For the massless case, $R_f(t)$ is known up to the three-loop level [22,28,29], while mass effects were evaluated to two loops in Ref. [20]. $E(t)$ only receives massive contributions at two loops and above, which have been considered in Ref. [30], with the massless case being taken to three loops [3,30]. At two-loop level, only a single diagram contributes to the mass effects of $E(t)$, shown in Fig. 2 (c).

3.2 Renormalization

Renormalization in the GFF is carried out in the usual way, with the renormalized fields and parameters being related to their bare counter parts by

$$
\begin{aligned}
B_\mu &= \sqrt{Z_B} B_{0\mu}\,, \qquad \alpha_s = \left(\frac{\mu^2 e^{\gamma_E}}{4\pi}\right)^\epsilon Z_\alpha \frac{g_0^2}{4\pi}\,, \\
\chi &= \sqrt{Z_\chi} \chi_0\,, \qquad m_f = Z_m m_{f0}\,, \\
\bar\chi &= \sqrt{Z_\chi} \bar\chi_0\,,
\end{aligned}
\tag{12}
$$

where the renormalization constants are Laurent series in the dimensional regularisation parameter $\epsilon = (4 - D)/2$, with D being the number of space-time dimensions which we adopt for the loop-momentum integration. As the flow time acts as a ultra-violet (UV) cutoff for the high momentum modes, additional operator renormalization is not required for flowed composite operators [4].

The coupling and mass renormalization constants are the same as in regular QCD. In the $\overline{\text{MS}}$ scheme, they read

$$
\begin{aligned}
Z_\alpha &= 1 - a_{4\pi} \frac{\beta_0}{2\epsilon} + a_{4\pi}^2 \left(\frac{3\beta_0^2}{8\epsilon^2} - \frac{\beta_1}{4\epsilon}\right) + \mathcal{O}(a_{4\pi}^3)\,, \\
Z_m^{\overline{\text{MS}}} &= 1 - a_{4\pi} \frac{\gamma_0^m}{\epsilon} + a_{4\pi}^2 \left[\frac{\gamma_0^m}{2\epsilon^2}(\gamma_0^m + \beta_0) - \frac{\gamma_1^m}{2\epsilon}\right] + \mathcal{O}(a_{4\pi}^3)\,,
\end{aligned}
\tag{13}
$$

with

$$
a_{4\pi}(\mu) = \frac{\alpha_s(\mu)}{4\pi}\,,
\tag{14}
$$

and

$$
\begin{aligned}
\beta_0 &= 11 - \frac{2}{3} N_F\,, \qquad \beta_1 = 102 - \frac{38}{3} N_F\,, \\
\gamma_0^m &= 4\,, \qquad\qquad\quad \gamma_1^m = \frac{202}{3} - \frac{20}{9} N_F\,.
\end{aligned}
\tag{15}
$$

As will become clear below, it is convenient to present our results with the quark mass renormalized in the on-shell scheme. In this case, the mass renormalization constant reads

$$
Z_m^{\text{OS}} = c_m Z_m^{\overline{\text{MS}}}\,,
\tag{16}
$$

7

with

$$c_m = 1 + a_{4\pi}\delta_m^{(1)} + a_{4\pi}^2\delta_m^{(2)} + \mathcal{O}(a_{4\pi}^3)\,, \tag{17}$$

and

$$\delta_m^{(1)} = \frac{16}{3} + 4\ln\frac{\mu^2}{\bar{m}^2(\mu)}\,,$$

$$\delta_m^{(2)} = 215.094 - 16.662N_{\mathrm{L}} + (109.556 - 5.778N_{\mathrm{L}})\ln\frac{\mu^2}{\bar{m}^2(\mu)} \tag{18}$$

$$+ (28.667 - 1.333N_{\mathrm{L}})\ln^2\frac{\mu^2}{\bar{m}^2(\mu)}\,.$$

where N_{L} is the number of massless quarks. The full analytic expressions are available in Ref. [31]. Since we evaluate the integrals numerically, we need to insert the mass counter terms at the integrand level and re-expand the corresponding propagators in the coupling constant as follows:

$$\frac{1}{p^2 + m_0^2} = \frac{1}{p^2 + m^2}\left(1 - \frac{\delta m^2}{p^2 + m^2} + \mathcal{O}\left(\delta m^2\right)\right)\,,$$

where $\delta m^2 = m^2(Z_m^2 - 1) = \mathcal{O}(\alpha_s)$. This means that we need to evaluate integrals with higher powers of the propagators, albeit only at lower loop orders, because each additional power is accompanied by a factor α_s. Such integrals can be calculated in the same way as described in Section 3.3 below.

While the flowed-gluon field renormalization can be set to [3, 4]

$$Z_B = 1\,, \tag{19}$$

the flowed-fermion field renormalization in the $\overline{\mathrm{MS}}$ scheme reads [22, 29]

$$Z_\chi^{\overline{\mathrm{MS}}} = 1 + a_{4\pi}\left[\frac{3C_{\mathrm{F}}}{\epsilon}\right] + a_{4\pi}^2\frac{C_{\mathrm{F}}}{2\epsilon}\left[\frac{3}{\epsilon}\left(3C_{\mathrm{F}} - \frac{11}{3}C_{\mathrm{A}} - \frac{4}{3}T_{\mathrm{R}}N_{\mathrm{F}}\right)\right.$$

$$\left. + C_{\mathrm{A}}\left(\frac{223}{6} - 8\ln 2\right) - C_{\mathrm{F}}\left(\frac{3}{2} + 8\ln 2\right) - \frac{22}{3}T_{\mathrm{R}}N_{\mathrm{F}}\right] + \mathcal{O}(a_{4\pi}^3)\,, \tag{20}$$

where $\gamma_{\mathrm{E}} \approx 0.5772$ is the Euler-Mascheroni constant, C_{F}, C_{A}, and T_{R} are the Casimir factors and the trace normalization of the gauge group; in QCD, it is

$$C_{\mathrm{F}} = \frac{4}{3}\,, \quad C_{\mathrm{A}} = 3\,, \quad \text{and} \quad T_{\mathrm{R}} = \frac{1}{2}\,. \tag{21}$$

Since the $\overline{\mathrm{MS}}$ scheme is intrinsically perturbative and we would like to be able to combine our results with the corresponding lattice results, it is preferable to adopt a non-minimal,

8

regularization-independent renormalization scheme for the fermions which leads to RG invariant quantities. One option is the so-called ringed scheme, defined as

$$\mathring{Z}_\chi \sum_f R_f(t) \bigg|_{m=0} \equiv -\frac{2n_c N_F}{(4\pi t)^2} \,, \tag{22}$$

with $n_c = 3$ the number of colors, $R_f(t)$ from Eq. (11), and

$$\mathring{Z}_\chi = \zeta_\chi \, Z_\chi^{\overline{\mathrm{MS}}} \,. \tag{23}$$

Through NNLO, the conversion factor reads [22, 29]

$$\begin{aligned}
\zeta_\chi &= 1 + a_{4\pi} \left(3\, C_F L_{\mu t} - 3\, C_F \ln 3 - 4\, C_F \ln 2 \right) \\
&\quad + a_{4\pi}^2 \left\{ \frac{C_F}{6} \left[C_A \left(-136 \ln 2 - 66 \ln 3 + 223 \right) + C_F \left(-120 \ln 2 \right. \right. \right. \\
&\qquad \left. \left. -54 \ln 3 - 9 \right) + T_R N_F \left(32 \ln 2 + 24 \ln 3 - 44 \right) \right] L_{\mu t}^2 \\
&\qquad + \frac{C_F}{2} \left(11\, C_A + 9\, C_F - 4\, T_R N_F \right) L_{\mu t} - 23.7947\, C_A C_F + 30.3914\, C_F^2 \\
&\qquad \left. - 3.9226\, C_F T_R N_F \right\}.
\end{aligned} \tag{24}$$

The renormalized quantities

$$\mathring{S}_f(t) = \mathring{Z}_\chi S_f(t) \quad \text{and} \quad \mathring{R}_f(t) = \mathring{Z}_\chi R_f(t) \tag{25}$$

are then RG invariant. These two quantities, together with the RG-invariant VEV of the action density, $E(t)$, are the main focus of this paper. Of course, they also allow one to evaluate the RG-invariant ratios

$$\begin{aligned}
r_{f,a}(t) &= \frac{S_f(t)}{R_f(t)} \,, \\
r_{f,b}(t) &= \frac{R_f(t)}{R_f(t)|_{m=0}} = -\frac{(4\pi t)^2}{2n_c} \mathring{R}_f(t) \,, \\
r_{f,c}(t) &= m_f \frac{d}{dm_f} r_{f,a}(t)
\end{aligned} \tag{26}$$

suggested in Ref. [20] for the quark-mass determination.

The bulk of our results is obtained under the assumption that there is one massive quark and $N_L = N_F - 1$ light quarks, where we focus on $N_F = 4$ and $N_F = 5$. When calculating S_f and R_f, we assume f to be the massive quark. The effect of a second massive quark will be briefly discussed at the end of Section 5.

9

3.3 Computation

Table 1: Number of integrals involving zero, one, and two masses, and the number of Feynman diagrams, split into LO, NLO, and NNLO for $S_f(t)$, $R_f(t)$ and $E(t)$.

	$S_f(t)$			$R_f(t)$			$E(t)$		
	LO	NLO	NNLO	LO	NLO	NNLO	LO	NLO	NNLO
zero masses	0	2	177	3	11	790	1	23	1990
one mass	3	30	978	1	47	1922	0	10	409
two masses	0	0	71	0	0	182	0	0	20
diagrams	1	8	258	1	11	377	1	17	419

As opposed to the NLO calculation [3, 20, 30, 32], the increased complexity at NNLO makes automation indispensible. Table 1 provides a breakdown of the number of diagrams and integrals that appear in the computation of each of the VEVs.[1] While this list provides an approximate view of the comparative computation cost in calculating each process, it does not reflect the increase in complexity by the inclusion of non-zero quark masses.

A general overview of the setup used in the computations in this paper can be found in Ref. [22], but in brief, computations proceed as in regular perturbation theory. We generate the necessary Feynman diagrams using `qgraf` [33, 34] and visualize them with the help of `FeynGame3` [23]; the Feynman rules are inserted using `tapir` [35] and `exp` [36] such that the Feynman integrals can be produced in the symbolic manipulation language `FORM` [37, 38]; the integrals are then evaluated. Due to the addition of an exponential smoothing term in the computation of processes involving flowed fields, the integrals to be evaluated are distinct from standard Feynman integrals. They are also highly structured though, allowing for integral reduction via integration-by-parts relations [22, 39]; `Kira+FireFly` [40–43] can be used for this purpose in principle. In our case, we find that the reduction is less efficient than a direct numerical evaluation of the integrals.

To be specific, the scalar integrals we encounter at l-loop level, for $l \leq 3$, are of the general form

$$f(\mathbf{c}, \mathbf{b}, \{\{n_1, m_1\}, \ldots, \{n_n, m_n\}, \{n_{1,2}, m_{1,2}\}, \ldots, \{n_{n-1,n}, m_{n-1,n}\}\}) =$$

$$= (4\pi t)^{\frac{ld}{2}} \int_0^1 \mathbf{u^c} d\mathbf{u} \prod_{i=1}^{n} \int_{k_i} \frac{\exp(-tb_i k_i^2)}{(t(k_i^2 + m_i^2))^{n_i}} \prod_{j>i}^{n} \frac{\exp(-tb_{i,j} k_{i,j}^2)}{(t(k_{i,j}^2 + m_{i,j}^2))^{n_{i,j}}} , \qquad (27)$$

where $k_{i,j}^2 = (k_i - k_j)^2$ with $b_{i,j}$, $n_{i,j}$ and $m_{i,j}$ being parameters associated with these momenta. Note that factors of the flow time are included to ensure the term is dimension-

---

[1]These numbers are supplied without any attempt to reduce them via integration-by-parts relations.

less, and the **b** parameters can be functions of the **u** parameters. The latter arise from contributions due to flowlines.

While the integrals in Eq. (27) can be evaluated analytically for $l = 1$, the exact solution at two loops is known only for special values of the parameters, in particular for the massless case $m_i = m_{i,j} = 0$ [29]. At three-loop level, even this case has not been fully solved. We therefore resolve to a numerical evaluation of the integrals.

A program designed specifically for this purpose is `ftint` [44]. It provides an interface to `pySecDec` [45] which applies sector decomposition and subsequent numerical integration of the integrals. The result is a Laurent series in ϵ with numerical coefficients. The cancellation of the pole terms in ϵ in the renormalized results to the numerical accuracy of the computation provides an obvious though non-trivial check of our results.

The sector decomposition of the integrals is independent of the specific mass values m_i and $m_{i,j}$. `ftint` allows one to separate this step from the subsequent numerical integration, which can then be performed for arbitrary values of the masses. This is particularly important since in our case the sector decomposition is typically more computationally expensive than the numerical integration.

4   Results

The main results of this paper constitute the numerically evaluated component values of the perturbative series of the VEVs defined in Eq. (11). Since we provide only numerical results for these quantities, we need to define an adequate range for the flow time. Its value should be distant from the limiting scales, given by the square of the lattice spacing a and size L, as well as $1/\Lambda_{\mathrm{QCD}}^2$ which is associated with the breakdown of perturbation theory. Following the conditions on the flow time t suggested by Ref. [20, 27],

$$a^2 \ll 8t \ll L^2, \qquad 8t \ll \Lambda_{\mathrm{QCD}}^{-2},$$
$$0.1 \ll 8\bar{m}_c^2 t \ll 20, \qquad 1.0 \ll 8\bar{m}_b^2 t \ll 200, \tag{28}$$

a set of 200 points considered between $0.001 \leq m^2 t \leq 63$ should be sufficient to cover our region of interest for both the case of the charm and the bottom quark. Note, often linear interpolation is used between points on this grid. In the following we will present these data in a form that is independent of the specific massive quark flavor under consideration.

11

4.1 The scalar quark density

Up to the perturbative order N, the VEV of the scalar quark density in the ringed scheme can be written as

$$\mathring{S}_f(t) = -\frac{n_c m_f}{8\pi^2 t} \sum_{n=0}^{N} a_{4\pi}^n(\mu) s_n(m_f, t, \mu), \qquad s_n(m, t, \mu) = \sum_{k=0}^{n} s_{n,k}(m^2 t) L_{\mu t}^k, \qquad (29)$$

where

$$L_{\mu t} = \ln 2\mu^2 t + \gamma_{\mathrm{E}}. \qquad (30)$$

The coefficients $s_{n,k}(m^2 t)$ are dimensionless. At NNLO, we further split them into

$$s_{2,k} = s_{2,k,0} + N_{\mathrm{L}} s_{2,k,1}, \qquad (31)$$

where N_{L} is the number of light (massless) quarks.

For simplicity of the presentation, let us assume for the moment that the mass m is renormalized in the on-shell scheme. We will provide the required conversion to the $\overline{\mathrm{MS}}$ scheme further below. Due to the RG invariance of $\mathring{S}_f$ and the fact that it starts at order α_s^0, a logarithmic term only appears at NNLO. It is given by the non-logarithmic NLO coefficient as

$$s_{2,1} = \beta_0 \, s_{1,0}, \qquad (32)$$

where β_0 is given in Eq. (15). The LO result can be obtained analytically [5, 26]:

$$s_{0,0}(z) = 1 - 2z \, e^{2z} \, \Gamma(0, 2z). \qquad (33)$$

Fig. 3 shows the non-logarithmic terms $s_{0,0}$, $s_{1,0}$, $s_{2,0,0}$, and $s_{2,0,1}$. For small $m^2 t$, the change in the components is generally very steep, where the overall process is expected to be linear in the mass value. It then flattens out for large mass where it is expected to vary as $1/m^2 t$. A comparison of the components of $s_{2,i,0}$ and $s_{2,i,1}$ suggests that the contributions from the secondary massless quarks appearing in loops is subdominant to the massive quark.

Switching to a different renormalization scheme for the quark mass can be achieved as follows. Assume that the relation between the on-shell mass m and the mass in the new scheme $\hat{m}$ is given by

$$m = \hat{m} \left(1 + a_{4\pi} \hat{\delta}_m^{(1)} + a_{4\pi}^2 \hat{\delta}_m^{(2)} + \ldots \right). \qquad (34)$$

For the $\overline{\mathrm{MS}}$ scheme, $\hat{m} = \bar{m}(\mu)$ and $\hat{\delta}_m^{(n)} = \delta_m^{(n)}$, see Eq. (18), for example. Then $\mathring{S}_f(t)$ is given by the same formulas as Eq. (29) with m_f replaced by $\hat{m}_f$, and s_n replaced by $\hat{s}_n$,
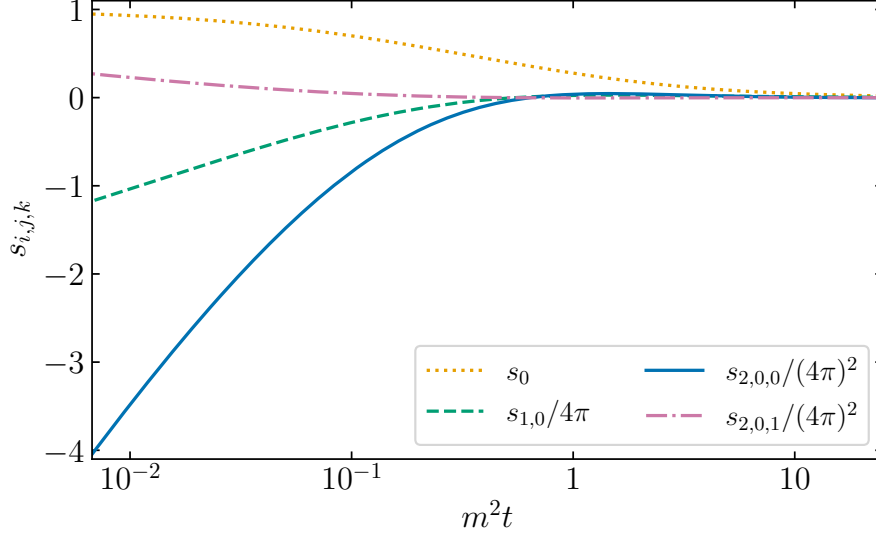
12

Figure 3: $L_{\mu t}$-independent components of $\mathring{S}_f(t)$ in the form of Eqs. (29) and (31).

where

$$
\begin{aligned}
\hat{s}_0 &= s_0\,, \\
\hat{s}_1 &= s_1 + \delta_m^{(1)} \left(s_0 + 2\hat{z}\, s_0'\right)\,, \\
\hat{s}_2 &= s_2 + \delta_m^{(1)} \left(s_1 + 2\hat{z}\, s_1'\right) + \delta_m^{(2)} \left(s_0 + 2\hat{z}\, s_0'\right) + \hat{z}\, (\delta_m^{(1)})^2 \left(3s_0' + 2\hat{z}\, s_0''\right)\,, \\
\hat{z} &= \hat{m}^2 t\,,
\end{aligned}
\tag{35}
$$

and

$$
s_{n,k}'(\hat{z}) = \frac{\mathrm{d}}{\mathrm{d}\hat{z}} s_{n,k}(\hat{z})\,.
\tag{36}
$$

Thus, in order to convert between different mass schemes, aside from the non-logarithmic terms, we also need the first and second derivative of the LO term, which is easily obtained from Eq. (33), as well as the first derivative of the NLO coefficient, which we provide in terms of a one-dimensional grid along with the non-logarithmic coefficients; it is also plotted in Fig. 4.
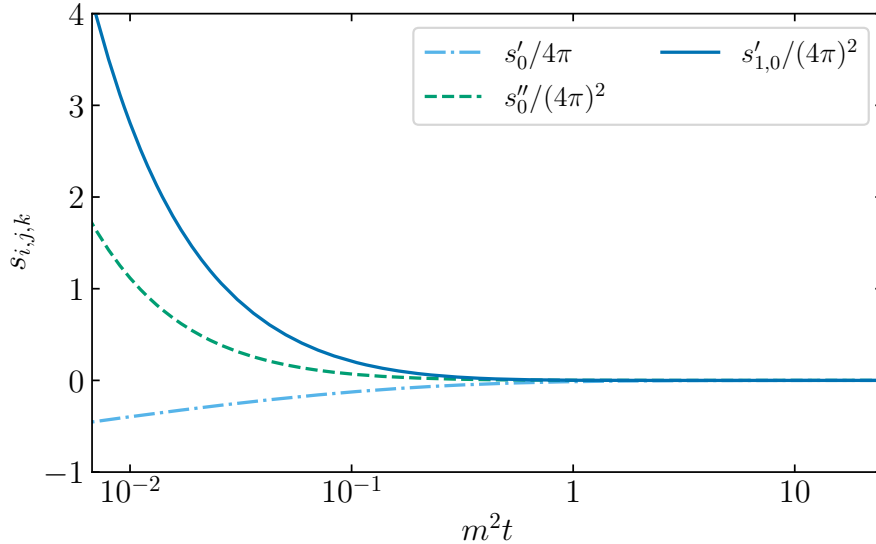
13

Figure 4: Derivatives of the $L_{\mu t}$-independent components of $\mathring{S}_f(t)$.

4.2 The quark kinetic density

In analogy to Eq. (29), we write the VEV of the quark kinetic density in the ringed scheme up to order N as

$$\mathring{R}_f(t) = -\frac{2n_{\mathrm{c}}}{(4\pi t)^2} \sum_{n=0}^{N} a_{4\pi}^n r_n(m_f, t, \mu) \,, \qquad r_n(m, t, \mu) = \sum_{k=0}^{n} r_{n,k}(m^2 t) L_{\mu t}^k \,. \tag{37}$$

Again, we further write

$$r_{2,k} = r_{2,k,0} + N_{\mathrm{L}}\, r_{2,k,1} \,. \tag{38}$$

As for $\mathring{S}_f$, a logarithmic term only appears at NNLO, and it can be expressed by the non-logarithmic NLO coefficient:

$$r_{2,1} = \beta_0\, r_{1,0} \,. \tag{39}$$

The LO coefficient is given by

$$r_{0,0}(z) = 1 - z + 4z^2\, e^{2z}\Gamma(0, 2z) \,. \tag{40}$$

The dimensionless coefficients $r_{0,0}$, $r_{1,0}$, $r_{2,0,0}$ and $r_{2,0,1}$ are plotted in Fig. 5.
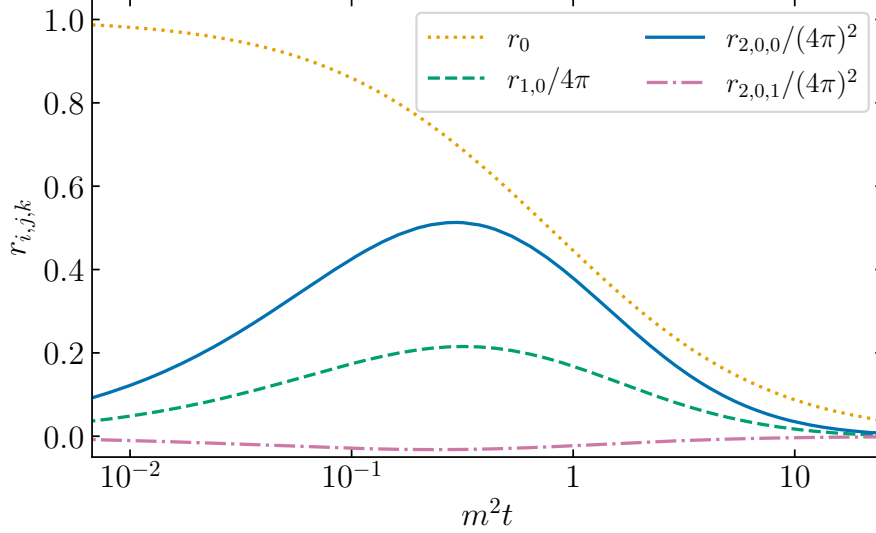
14

Figure 5: $L_{\mu t}$-independent components of $\mathring{R}_f(t)$ in the form Eq. (37).

The conversion to another mass scheme as defined in Eq. (34) in this case is obtained by replacing m by $\hat{m}$ and r_n by $\hat{r}_n$, where

$$
\begin{aligned}
\hat{r}_0 &= r_0 \,, \\
\hat{r}_1 &= r_1 + 2\,\delta_m^{(1)}\hat{z}\,r_0' \,, \\
\hat{r}_2 &= r_2 + 2\,\delta_m^{(1)}\hat{z}\,r_1' + \hat{z}\left((\delta_m^{(1)})^2 + 2\,\delta_m^{(2)}\right)r_0' + 2(\delta_m^{(1)})^2\hat{z}^2 r_0'' \,.
\end{aligned}
\tag{41}
$$

The derivatives r_0', $r_1' = r_{1,0}'$, and r_0'' are shown in Fig. 6.

4.3   The action density

The VEV of the action density $E(t)$ is expanded as

$$
E(t) = \frac{3\alpha_s}{4\pi t^2}\frac{n_{\mathrm{A}}}{8}\sum_{n=0}^{N} a_{4\pi}^n e_n(m,t,\mu)\,, \qquad e_n(m,t,\mu) = \sum_{k=0}^{n} e_{n,k}(m^2 t)L_{\mu t}^k\,,
\tag{42}
$$

where $n_{\mathrm{A}} = n_{\mathrm{c}}^2 - 1 = 8$ is the dimension of the adjoint representation of SU(3). In this case, already the NLO coefficients depend on the number of light fermions, so we write

$$
e_{1,k} = e_{1,k,0} + N_{\mathrm{L}}\,e_{1,k,1}\,, \qquad e_{2,k} = e_{2,k,0} + N_{\mathrm{L}}\,e_{2,k,1} + N_{\mathrm{L}}^2\,e_{2,k,2}\,.
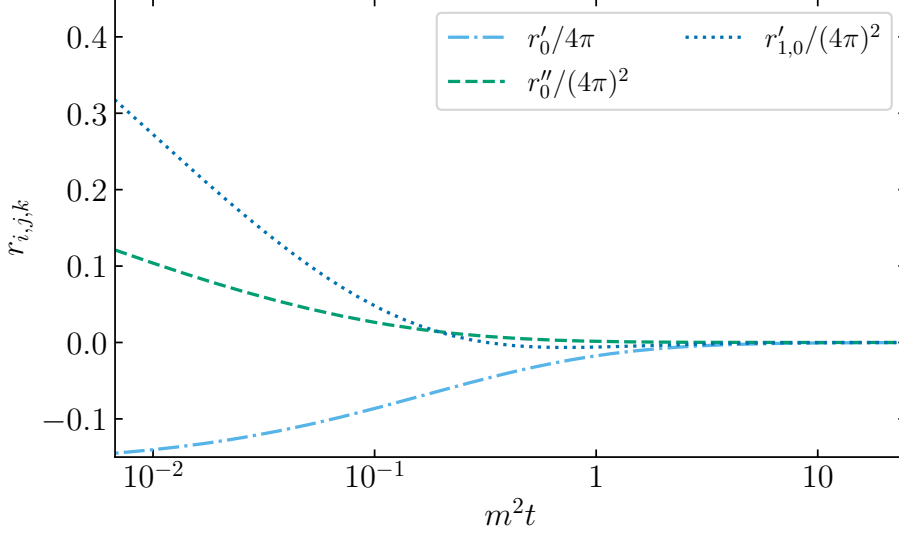\tag{43}
$$

15

Figure 6: m^2t derivatives of $L_{\mu t}$-independent components of $\mathring{R}_f(t)$.

Since $E(t)$ starts at order α_s, logarithmic terms appear already at NLO. They can be expressed in terms of the lower-order non-logarithmic terms as

$$e_{1,1} = \beta_0 e_{0,0}\,, \qquad e_{2,1} = \beta_1 e_{0,0} + 2\beta_0 e_{1,0}\,, \qquad e_{2,2} = 2\beta_0^2 e_{0,0}\,,$$
$$e_{n,k} = 0 \quad \text{otherwise, for} \quad n \leq 2 \,\wedge\, k \geq 1\,, \tag{44}$$

where β_0 and β_1 are given in Eq. (15). The LO result is simply given by

$$e_{0,0}(z) = 1\,. \tag{45}$$

The coefficient of the highest power of N_{L} at each order in α_s is a constant in m^2t. These values can be directly compared to the corresponding massless coefficients in Refs. [3,22,30]

$$e_{1,0,1} = -\frac{4}{9} \qquad \text{and} \qquad e_{2,0,2} = -\frac{20}{81} + \frac{2\pi^2}{27}\,. \tag{46}$$

The other independent components, $e_{1,0,0}$, $e_{2,0,0}$ and $e_{2,0,1}$ are plotted in Fig. 7.

Conversion from the on-shell to the $\overline{\mathrm{MS}}$ mass is particularly simple in this case:

$$\hat{e}_0 = e_0\,, \qquad \hat{e}_1 = e_1\,, \qquad \hat{e}_2 = e_2 + 2\,\delta_m^{(1)}\hat{z}\,e_1'\,. \tag{47}$$

The only mass-dependent component of e_1', $e_{1,0,0}'$ is also plotted in Fig. 7.
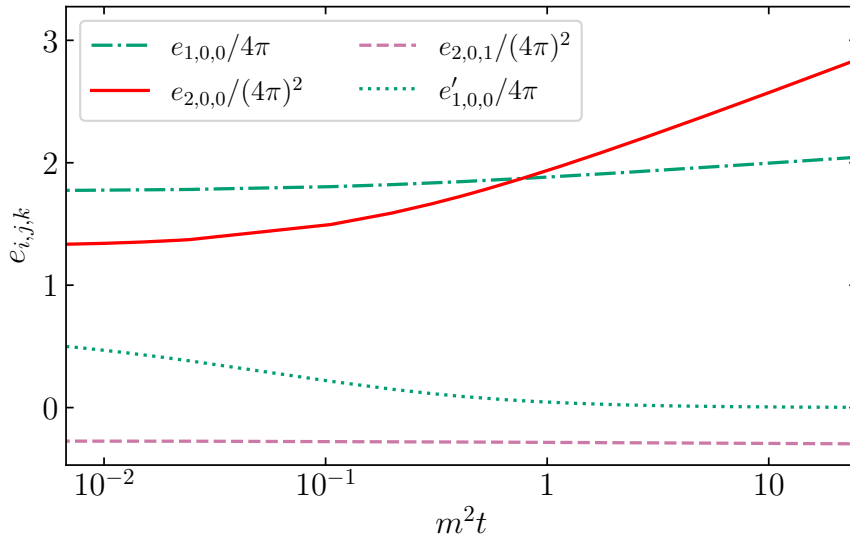
16

Figure 7: Components of $E(t)$ in the form Eq. (42) and its m^2t derivatives of $L_{\mu t}$-independent components.

5   Phenomenological results

While in Sections 4.1 to 4.3, we provided the individual components of the VEVs as functions of m^2t, we will now combine them in order to obtain numerical values for the complete VEVs up to NNLO QCD. In particular, we will estimate their theoretical accuracy by varying the renormalization scale.

As pointed out above, we will consider the cases of QCD with $N_F = 4$ and $N_F = 5$ quark flavors, where $N_F - 1$ quarks are taken to be massless, so that the mass effects only arise from the heaviest quark. Thus, for $N_F = 4$ ($N_F = 5$), we will only consider $S_f(t)$ and $R_f(t)$ for $f = c$ ($f = b$), cf. Eq. (11). We will briefly study the effect of a second massive quark at the end of this section.

Throughout this paper, our input value for the strong coupling is

$$\alpha_s(M_Z) = 0.118 \quad \text{with} \quad M_Z = 91.188 \, \text{GeV} . \tag{48}$$

For the numerical results, we renormalize the quark mass in the $\overline{\text{MS}}$ scheme, using

$$\bar{m}_c(\bar{m}_c) = 1.273 \, \text{GeV} \quad \text{and} \quad \bar{m}_b(\bar{m}_b) = 4.183 \, \text{GeV} \tag{49}$$

17

as input values [14]. For each of these masses, we follow Ref. [20] and define a central renormalization scale

$$\mu_{\text{int}} = \sqrt{\mu_t^2 + \bar{m}^2(\bar{m})}, \quad \text{where} \quad \mu_t = \frac{\exp(-\frac{\gamma_{\text{E}}}{2})}{\sqrt{2t}}, \tag{50}$$

which aims at avoiding large logarithms emerging due to the difference between the quark mass and the flow time. For the case of the gluon condensate $E(t)$, the central scale μ_t is used since the contributions from the quark mass first appear at the two loop level, as such the logarithms from the mass scale are suppressed.
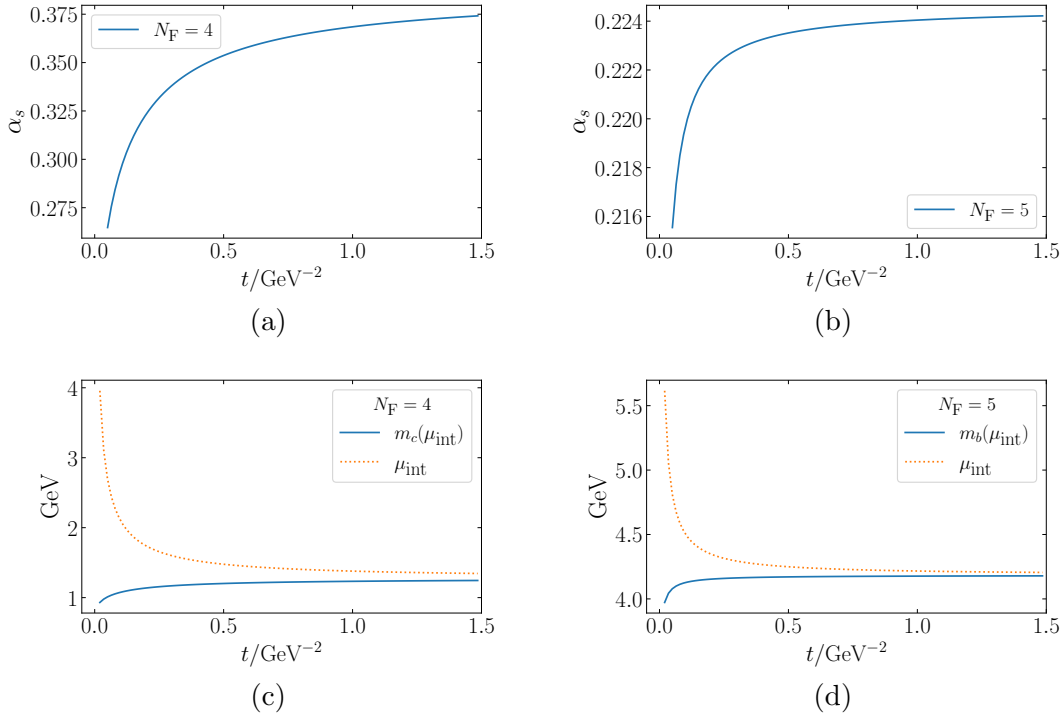
(a)

(b)

(c)

(d)

Figure 8: Upper row (a/b): $\alpha(\mu_{\text{int}})$. Lower row (c/d): $m_f(\mu_{\text{int}})$ (solid) and μ_{int} (dotted). Left column (a/c): $N_{\text{F}} = 4$; right column (b/d): $N_{\text{F}} = 5$.

For each quantity, α_s is evolved from the reference scale M_Z to the central scale μ_{int} at the five-loop level. When working in the ($N_{\text{F}} = 4$)-flavor theory, we use the four-loop decoupling relations for α_s at $\mu = \bar{m}_b(\bar{m}_b)$. Similarly, we evolve the quark masses from $\bar{m}(\bar{m})$ to $\bar{m}(\mu_{\text{int}})$ at five-loop level. To provide an understanding of the scales we are considering, in Fig. 8 we plot the running coupling constant (upper row) and the running

18

charm and bottom mass (lower row) as functions of the flow time t, both for $N_{\mathrm{F}} = 4$ (left) and $N_{\mathrm{F}} = 5$ (right) as a function of t. These plots demonstrate the regularization of non-perturbative behavior which occurs in the massless limit towards large t. Due to the occurrence of the quark mass in μ_{int}, the coupling and the quark mass tend towards constants in this limit.

5.1   Size of the mass effects

One of the primary purposes of this work is to evaluate the importance of the quark-mass effects in these gradient-flow quantities. The first question we will ask therefore is how the VEVs compare to their massless equivalents. For the case of $E(t)$ and $R_f(t)$ we will simply use the massless values of the series. However, since $S_f(t) \propto m_f$, the naïve massless equivalent vanishes. Instead, we will consider

$$\mathring{S}_f^{\mathrm{ML}}(t) = m_f \left[\frac{d\mathring{S}_f(t)}{dm_f} \bigg|_{m_f = 0} \right]. \tag{51}$$

This quantity is used in Ref. [22] to define the gradient-flow mass; it is equivalent to the leading term in the small-mass expansion. Fig. 9 compares successively higher perturbative orders of this massless limit to the leading-order result which, however, includes the full mass dependence. It shows that the quark-mass effects are considerably larger than the radiative corrections already at rather small values of t. In fact, as noted in Ref. [20], even including higher terms in an expansion around the small-mass limit has only a very limited range of applicability.

The analogous comparison for $\mathring{R}_f$ is shown in the lower row of Fig. 9. By definition of the ringed scheme, there are no higher-order corrections in the massless limit in this case, see Eq. (22). The relative size of the LO mass effects is comparable to those in $\mathring{S}_f$. Fig. 9 (c) and (d) also include higher orders for the full massive results. Compared to the LO mass effects as well as to the radiative corrections in the massless case, we find these corrections to be very moderate. They will be studied in more detail below for all VEVs under consideration.

Finally, Fig. 10 compares $E(t)$ including the full quark-mass dependence to the case of purely massless quarks. In this case, there are no mass effects in the LO result as is obvious from the contributing Feynman diagrams, see Fig. 1. While the mass effects at NLO are quite moderate, amounting to less than 4% below $t = 0.5/\mathrm{GeV}^2$ in the case of a massive charm quark (and $N_{\mathrm{F}} = 4$, Fig. 10 (a)), they reach up to 15% at NNLO. In the ($N_{\mathrm{F}} = 5$)-case with a massive bottom quark, these numbers are 6% and 20%, respectively, see Fig. 10 (b).
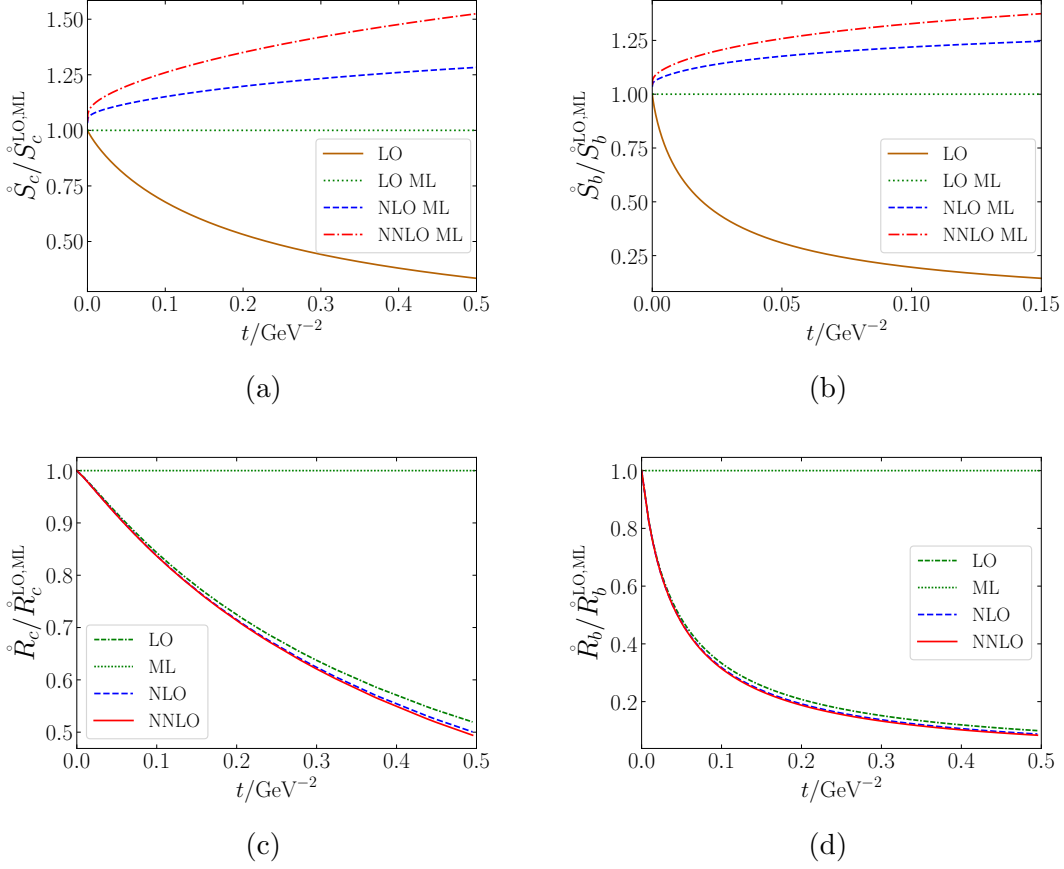
Figure 9: Upper row (a/b): $\mathring{S}_f/\mathring{S}_f^{\mathrm{LO,ML}}$, where $\mathring{S}_f$ is taken in the "massless" limit (ML, cf. Eq. (51)) at LO, NLO, and NNLO perturbation theory (dotted, dashed, dash-dotted), and the LO result including effects from non-zero m_f (solid); left (a/c): $f = c$, right (b/d): $f = b$. Lower row (c/d): analogous results for $\mathring{R}_f/\mathring{R}_f^{\mathrm{LO,ML}}$; note that in this case, higher perturbative orders in the massless case are zero by definition of the ringed scheme; instead, the NLO and NNLO curves are included here, evaluated at the central scale μ_{int}.

5.2 Radiative corrections

Let us now study the radiative corrections to the VEVs when the full mass effects are included. In particular, we want to address the residual perturbative uncertainty estimated by varying the renormalization scale. For this variation, we evolve the mass and the
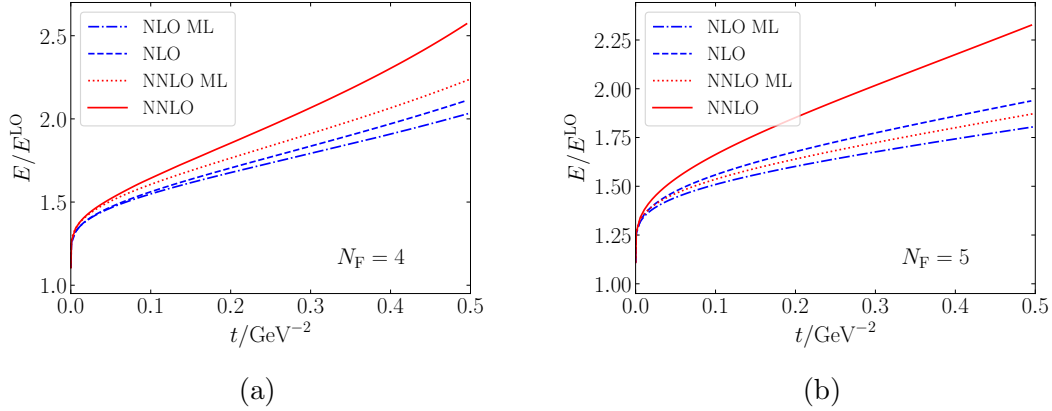
Figure 10: E/E^{LO} for $N_{\text{F}} = 4$ (left) and $N_{\text{F}} = 5$ (right) at NLO and NNLO with either one or zero massive quarks.

coupling according to the perturbative order of the VEVs. As in both $\mathring{S}_f(t)$ and $\mathring{R}_f(t)$ the mass appears at LO, we evolve $m(\mu_{\text{int}})$ to $m(\mu)$ at N-loop level when considering these quantities at N-loop order ($N = 1, 2, 3$). On the other hand, α_s first appears at NLO, which is why we evolve $\alpha_s(\mu_{\text{int}})$ to $\alpha_s(\mu)$ only at $(N-1)$-loop level. For $E(t)$, on the other hand, the situation is reversed: the coupling appears at LO and the mass only at NLO, so we evolve α_s at N-loop level and the mass at $(N-1)$-loop level in this case. All running and decoupling calculations are done with the help of `RunDec` [46–48].

For each value in t, the scale μ is varied in the range

$$\mu \in \Delta_\mu = [\mu_{\text{int}}/2, 2\,\mu_{\text{int}}]. \tag{52}$$

For a measurable quantity ρ, the limits of the scale envelope are the maximum and minimum values in this range, i.e. for each value of t, it is

$$\rho = \rho_0{}^{+\delta\rho_+}_{-\delta\rho_-} \tag{53}$$

where

$$\rho_0 = \rho|_{\mu=\mu_{\text{int}}}, \qquad \delta\rho_+ = \max_{\mu\in\Delta_\mu} \rho - \rho_0, \qquad \delta\rho_- = \rho_0 - \min_{\mu\in\Delta_\mu} \rho, \tag{54}$$

The upper row of Fig. 11 displays $\mathring{S}_f(t)$, evaluated at various loop orders and normalized to the LO expression taken at the central scale μ_{int}. The shaded regions indicate the perturbative uncertainties as given by Eq. (53). In the left plot, Fig. 11 (a), we consider $\mathring{S}_c(t)$ in the four-flavor theory ($N_{\text{F}} = 4$), keeping only the charm-quark mass different from
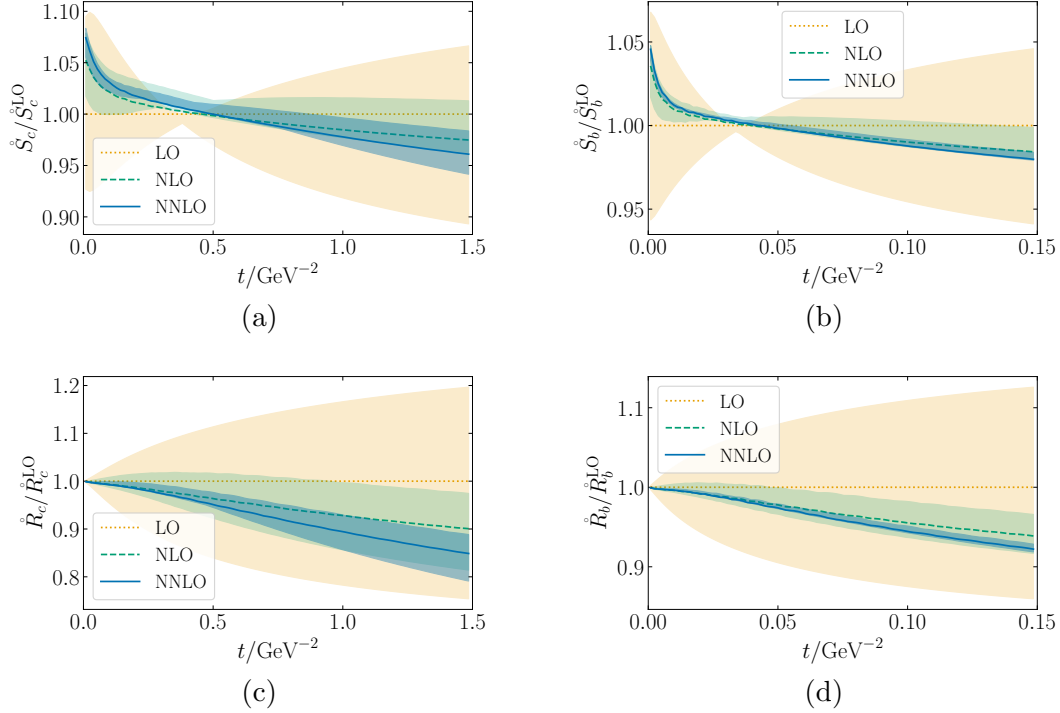
Figure 11: Upper row (a/b): $\mathring{S}_f/\mathring{S}_f^{\mathrm{LO}}$ at NLO and NNLO, including full quark-mass effects, with an envelope error formed by scale variation, see Eqs. (52) to (54). Lower row (c/d): The analogous plots for $\mathring{R}_f/\mathring{R}_f^{\mathrm{LO}}$. Left column (a/c): $f = c$, i.e. $N_{\mathrm{F}} = 4$ and massive charm quark; right column (b/d): $f = b$, i.e. $N_{\mathrm{F}} = 5$ and massive bottom quark.

zero. The right plot shows $\mathring{S}_b(t)$ for $N_{\mathrm{F}} = 5$, and only the bottom quark is considered massive. The expected reduction of the theoretical uncertainty when going to higher orders is particularly apparent in the case of $N_{\mathrm{F}} = 5$. Note that we use different ranges of t because our choice of the central scale μ_{int} depends on the mass of the massive fermion.

In general, the NNLO corrections lead to a considerable reduction of the theoretical uncertainty in both cases. While for the charm quark case, the uncertainty bands of the successive orders overlap over the whole range in t shown in the plots, the NLO and NNLO bands become slightly incompatible in the case of the bottom quark for $t \gtrsim 0.6\,\mathrm{GeV}^{-2}$, albeit still to an acceptable extent. The analogous plots for $\mathring{R}_f/\mathring{R}_f^{\mathrm{LO}}$ are shown in the lower row of Fig. 11. For $m_f \to 0$ (and thus $t \to 0$), the ratio tends to 1 in this case due to the definition of the ringed scheme.
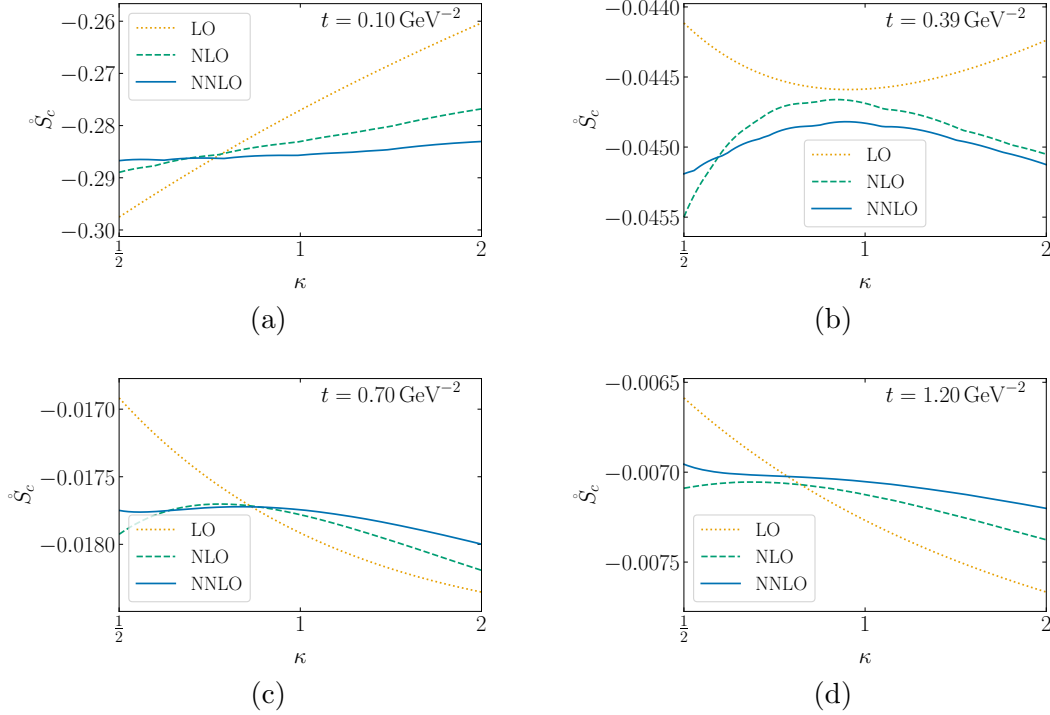
Figure 12: $\mathring{S}_c$ plotted across a range of $\kappa = \mu/\mu_{\text{int}}$ for various values of the flow time t.

While both for $\mathring{S}_f$ and $\mathring{R}_f$, a clear reduction of the scale uncertainty towards higher orders is observed, we should mention a qualitative difference between these two cases which is apparent from Fig. 11. For $\mathring{S}_f$, one observes a throat in the LO data at around $t \approx 0.4\,\text{GeV}^{-2}$, both for $f = c$ and $f = b$. It occurs because the $\mathcal{O}(a_s)$ coefficient to the scale variation vanishes due to a cancellation between the s_0 and s'_0 contributions, cf. Eq. (35). We consider this in more detail in Fig. 12 for $f = c$. Defining $\kappa = \mu/\mu_{\text{int}}$, it shows $\mathring{S}_c(t)$ for four different values of the flow time, $t \in \{0.1,\ 0.39,\ 0.7,\ 1.2\}\,\text{GeV}^{-2}$. In each case, the reduction in scale dependence of the observable is most apparent between LO and NLO, with a slight but noticeable improvement at NNLO. Note that across the throat, the direction of the scale variation changes; at the throat, the LO estimate of the uncertainty band is disjoint from those at higher orders.

For comparison, we provide the analogous plots for $\mathring{R}_f$ in Fig. 13. In this case, the qualitative scale dependence hardly changes between the different values of t, in keeping with the monotonous scale variation bands observed in Fig. 11 (c) and (d).
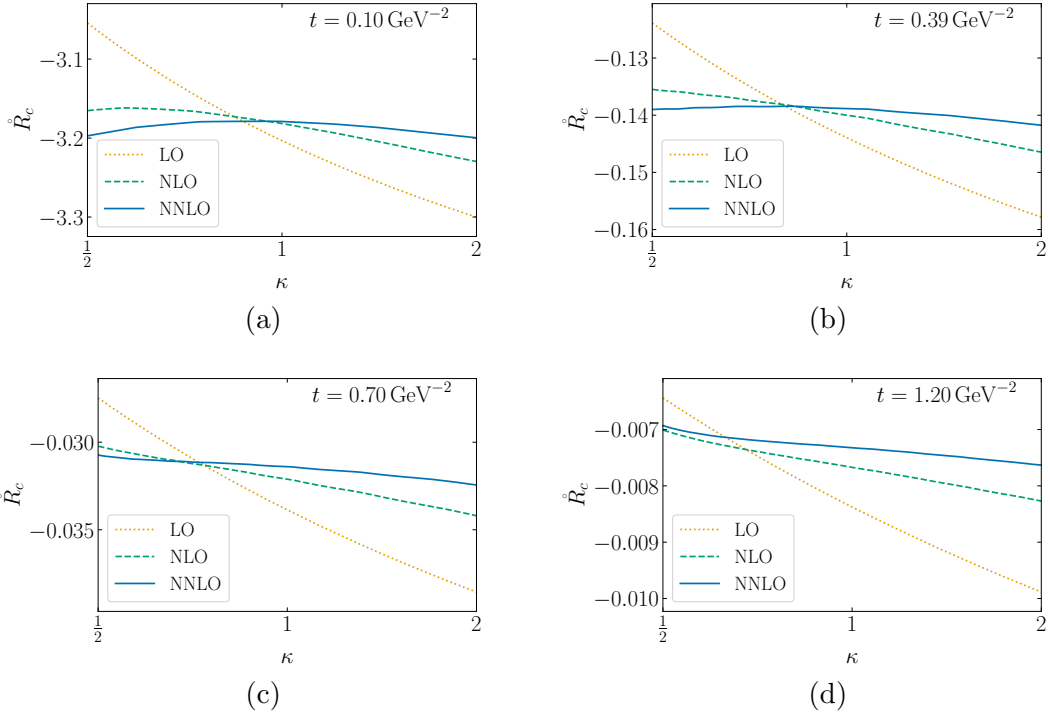
23

Figure 13: $\mathring{R}_c$ plotted across a range of $\kappa = \mu/\mu_{\text{int}}$ for various values of the flow time t.
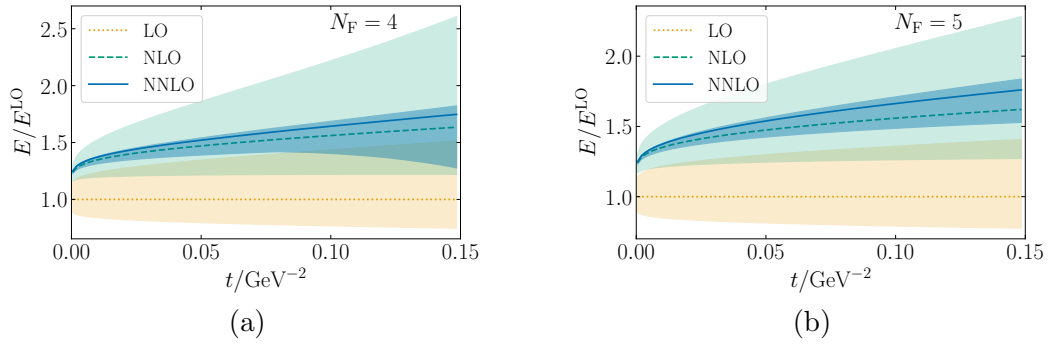

Figure 14: E/E^{LO} for (a) $N_{\text{F}} = 4$ (massive charm) and (b) $N_{\text{F}} = 5$ (massive bottom) at NLO and NNLO, with an envelope error formed by scale variation.
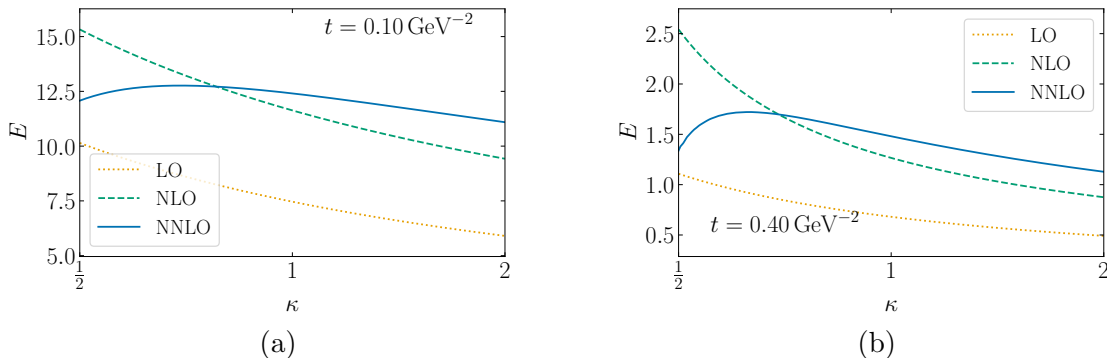
Figure 15: E for $N_\mathrm{F} = 5$ plotted across a range of $\kappa = \mu/\mu_t$ for (a) $t = 0.1\,\mathrm{GeV}^{-2}$ and (b) $t = 0.4\,\mathrm{GeV}^{-2}$.

We can perform a similar analysis on $E(t)$. However, in this case we decided to use μ_t rather than μ_int as the central scale, because the quark masses play only a secondary role of this quantity. This is apparent from the fact that, on the one hand, the LO expression for $E(t)$ is independent of the quark mass, and the mass effects at higher orders are significantly smaller than for the quark operators $\mathring{S}_f(t)$ and $\mathring{R}_f(t)$. Due to this choice of the central scale, the range of perturbative reliability in t is diminished though. In Fig. 14 we restrict the flow time to $t \leq 0.15\,\mathrm{GeV}^{-2}$, corresponding to $\mu_t \geq 1.37\,\mathrm{GeV}$, where the scale uncertainty at NNLO starts to increase, signaling the end of perturbative reliability. This can also be seen in Fig. 15 which considers the scale variation for a which uses larger t values.

5.3   Effects from a second quark mass

As discussed above, up to now we have only considered a single quark as massive, while the mass of the $N_\mathrm{F} - 1$ remaining ones was set to zero. In the remainder of this section, let us study the validity of this approximation by allowing for a second massive quark. For this discussion, we use μ_t as the central scale, cf. Eq. (50).

Additional massive quarks occur as insertions into gluon propagators, and higher-order corrections to that. For $R_f(t)$ and $S_f(t)$ such diagrams only appear at NNLO, while for $E(t)$ they occur at NLO in diagrams such as that shown in Fig. 2 (d). Our main concern here is to keep both m_c and m_b different from zero. Since in $E(t)$ the masses occur symmetrically, to a good approximation one can obtain the mass effects for two massive quarks by simply adding the mass effects of Fig. 10 (a) and (b). This neglects effects

25

arising from the different values of N_F in both plots, as well as NNLO contributions from diagrams which contain loop insertions from both massive quarks.
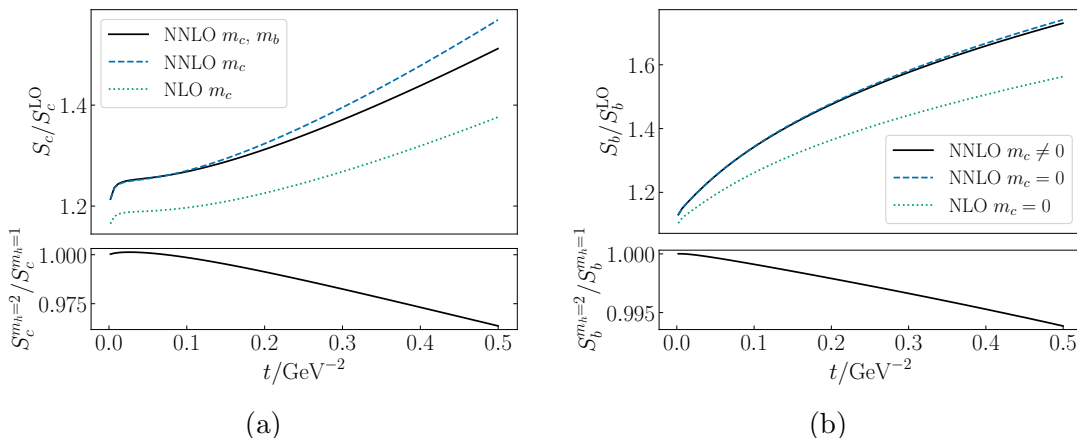

Figure 16: Effects of (a) a massive bottom quark on $\mathring{S}_c$, and (b) a massive charm quark on $\mathring{S}_b$. We have set $N_F = 5$ in both cases.

Concerning $\mathring{S}_f$ and $\mathring{R}_f$, the two massive quarks do not appear symmetrically and one needs to distinguish $f = c$ and $f = b$. We study these two cases for $\mathring{S}_f$ explicitly in Fig. 16. It compares the two-mass case to the LO, NLO and NNLO results for one massive quark. The change due to the additional quark masses clearly represents a sub-dominant contribution when compared with the jump from NLO to NNLO. Within the displayed range of the flow time, the contribution from the additional quark mass is less than the scale uncertainty in both cases, cf. Fig. 11. However, while the charm-quark mass effects on $\mathring{S}_b$ are at the sub-percent level, they do reach around 3% for the presence of a massive bottom quark in $\mathring{S}_c$. We find similar results for $\mathring{R}_f$, but refrain from showing them here.

6 Conclusions

Using the GFF within perturbation theory, we have presented results for the vacuum expectation values for phenomenologically relevant quark and gluon operators in QCD. These have been computed numerically for one massive and N_L massless quarks, with the flow-time integrals being evaluated for a set of points in the range $0.001 < m^2 t \leq 63$. We provide the numerical data in an ancillary file accompanying this paper.

As discussed in Ref. [20], two of these quantities, $S_f(t)$ and $R_f(t)$, provide the potential

to extract renormalized quark masses by comparing the perturbative results to lattice measurements. In the small-mass approximation, radiative corrections to these quantities have been obtained through NNLO. Since they were found to be substantial, it is important to control these corrections also in the case of massive quarks. Compared to the leading-order mass effects, however, we find that the radiative corrections on S_f and R_f are very modest. The perturbative prediction for these quantities is therefore under very good control.

The quantity $E(t)$ can be used to define a renormalization scheme for the strong coupling which can be implemented both on the lattice and within perturbation theory [49], for example, or to eliminate perturbative renormalon contributions in predictions for physical observables [50]. Computations on the lattice require finite quark masses, therefore a consistent comparison to perturbation theory requires the latter to include quark masses as well. In Fig. 10, we showed the change due to massive quarks can be relevant, particularly at NNLO.

This project has been focused on the computation of the mass effects of several VEVs which are fundamental to QCD in the gradient flow. Using the numerical data supplied with this paper in an ancillary file, it is straightforward to evaluate ratios as suggested in Ref. [20] for the extraction of the quark masses. One may also use these data to evaluate derivatives of these quantities w.r.t. the quark mass, as this eliminates non-perturbative effects that could spoil the mass determination. However, such a numerical derivative is quite sensitive to the accuracy and density of the original data. Alternatively, one could take the derivatives before loop integration. However, at NNLO this will lead to additional and significantly more complicated integrals. We therefore consider this beyond the scope of this work.

A   Ancillary file

We provide numerical results for the components defined in Sections 4.1 to 4.3 as `numpy` arrays in the ancillary `python` file `DataFile.py`. The naming scheme for the arrays encoding

$\mathring{S}_f(t)$ is

$$
\begin{aligned}
s_0 &\mathrel{\hat{=}} \texttt{s0RSOS} \\
s_{i,j} &\mathrel{\hat{=}} \texttt{s<i><j>RSOS} \\
s_{i,j,k} &\mathrel{\hat{=}} \texttt{s<i><j><k>RSOS} \\
s'_0 &\mathrel{\hat{=}} \texttt{s0pRSOS} \\
s'_{i,j} &\mathrel{\hat{=}} \texttt{s<i><j>pRSOS} \\
s''_0 &\mathrel{\hat{=}} \texttt{s0ppRSOS}
\end{aligned}
\tag{55}
$$

and similar for $\mathring{R}_f(t)$ and $E(t)$. For $\mathring{S}_f$ and $\mathring{R}_f$, these are one-dimensional arrays of length 249; the corresponding values of $m^2 t$ are given in the `numpy` array `m2tSR`. The arrays for $E(t)$ have length 200; the corresponding values for $m^2 t$ are provided in the `numpy` array `m2tE`.

For example, plotting s'_{10} vs. $m^2 t$ corresponds to the pseudo code `plot(m2tSR,s10pRSOS)`. The analogous command for plotting $e_{2,0,0}$ is `plot(m2tE,e200RSOS)`.

References

[1] R. Narayanan and H. Neuberger, "Infinite N phase transitions in continuum Wilson loop operators," *JHEP* **03** (2006) 064, `arXiv:hep-th/0601210`.

[2] M. Lüscher, "Trivializing maps, the Wilson flow and the HMC algorithm," *Commun. Math. Phys.* **293** (2010) 899–919, `arXiv:0907.5491 [hep-lat]`.

[3] M. Lüscher, "Properties and uses of the Wilson flow in lattice QCD," *JHEP* **08** (2010) 071, `arXiv:1006.4518 [hep-lat]`. [Erratum: JHEP 03, 092 (2014)].

[4] M. Lüscher and P. Weisz, "Perturbative analysis of the gradient flow in non-abelian gauge theories," *JHEP* **02** (2011) 051, `arXiv:1101.0963 [hep-th]`.

[5] M. Lüscher, "Chiral symmetry and the Yang–Mills gradient flow," *JHEP* **04** (2013) 123, `arXiv:1302.5246 [hep-lat]`.

[6] **BMW collaboration** Collaboration, S. Borsányi, S. Dürr, Z. Fodor, C. Hoelbling, S. D. Katz, S. Krieg, T. Kurth, L. Lellouch, T. Lippert, and C. McNeile, "High-precision scale setting in lattice QCD," *JHEP* **09** (2012) 010, `arXiv:1203.4469 [hep-lat]`.

[7] **Flavour Lattice Averaging Group (FLAG)** Collaboration, Y. Aoki *et al.*, "FLAG Review 2024," `arXiv:2411.04268 [hep-lat]`.

[8] A. Suzuki, Y. Taniguchi, H. Suzuki, and K. Kanaya, "Four quark operators for kaon bag parameter with gradient flow," *Phys. Rev. D* **102** no. 3, (2020) 034508, `arXiv:2006.06999 [hep-lat]`.

[9] M. Black, R. Harlander, F. Lange, A. Rago, A. Shindler, and O. Witzel, "Using gradient flow to renormalise matrix elements for meson mixing and lifetimes," *PoS* **LATTICE2023** (2024) 263, `arXiv:2310.18059 [hep-lat]`.

[10] H. Suzuki, "Energy–momentum tensor from the Yang–Mills gradient flow," *PTEP* **2013** (2013) 083B03, `arXiv:1304.0533 [hep-lat]`. [Erratum: PTEP 2015, 079201 (2015)].

[11] **WHOT-QCD** Collaboration, Y. Taniguchi, S. Ejiri, K. Kanaya, M. Kitazawa, H. Suzuki, and T. Umeda, "$N_f = 2+1$ QCD thermodynamics with gradient flow using two-loop matching coefficients," *Phys. Rev. D* **102** no. 1, (2020) 014510, `arXiv:2005.00251 [hep-lat]`. [Erratum: Phys.Rev.D 102, 059903 (2020)].

[12] A. Shindler, "Moments of parton distribution functions of any order from lattice QCD," *Phys. Rev. D* **110** no. 5, (2024) L051503, `arXiv:2311.18704 [hep-lat]`.

[13] A. Francis *et al.*, "Gradient flow for parton distribution functions: first application to the pion," `arXiv:2509.02472 [hep-lat]`.

[14] **Particle Data Group** Collaboration, S. Navas *et al.*, "Review of particle physics," *Phys. Rev. D* **110** no. 3, (2024) 030001.

[15] A. Hasenfratz, C. T. Peterson, J. van Sickle, and O. Witzel, "Λ parameter of the SU(3) Yang-Mills theory from the continuous β function," *Phys. Rev. D* **108** no. 1, (2023) 014502, `arXiv:2303.00704 [hep-lat]`.

[16] C. H. Wong, S. Borsanyi, Z. Fodor, K. Holland, and J. Kuti, "Toward a novel determination of the strong QCD coupling at the Z-pole," *PoS* **LATTICE2022** (2023) 043, `arXiv:2301.06611 [hep-lat]`.

[17] G. Schierholz, "QCD lambda parameter from gradient flow," *Eur. Phys. J. C* **85** no. 9, (2025) 1007, `arXiv:2410.17677 [hep-lat]`.

[18] R. Larsen, S. Mukherjee, P. Petreczky, H.-T. Shu, and J. H. Weber, "Scale setting and strong coupling determination in the gradient flow scheme for 2+1 flavor lattice QCD," `arXiv:2502.08061 [hep-lat]`.

[19] M. D. Brida, R. Höllwieser, F. Knechtli, T. Korzec, A. Ramos, S. Sint, and R. Sommer, "The strength of the interaction between quarks and gluons," `arXiv:2501.06633 [hep-ph]`.

[20] H. Takaura, R. V. Harlander, and F. Lange, "A new approach to quark mass determination using the gradient flow," *JHEP* **09** (2025) 025, `arXiv:2506.09537 [hep-lat]`.

[21] M. Black, R. V. Harlander, A. Hasenfratz, A. Rago, and O. Witzel, "Renormalized quark masses using gradient flow," `arXiv:2506.16327 [hep-lat]`.

[22] J. Artz, R. V. Harlander, F. Lange, T. Neumann, and M. Prausa, "Results and techniques for higher order calculations within the gradient-flow formalism," *JHEP* **06** (2019) 121, `arXiv:1905.00882 [hep-lat]`. [Erratum: JHEP 10, 032 (2019)].

[23] L. Bündgen, R. V. Harlander, S. Y. Klein, and M. C. Schaaf, "FeynGame 3.0" *Comput. Phys. Commun.* **314** (2025) 109662, `arXiv:2501.04651 [hep-ph]`.

[24] R. Harlander, S. Y. Klein, and M. C. Schaaf, "FeynGame-2.1 – Feynman diagrams made easy," *PoS* **EPS-HEP2023** (2024) 657, `arXiv:2401.12778 [hep-ph]`.

[25] R. V. Harlander, S. Y. Klein, and M. Lipp, "FeynGame," *Comput. Phys. Commun.* **256** (2020) 107465, `arXiv:2003.00896 [physics.ed-ph]`.

[26] R. Harlander, "The gradient flow at higher orders in perturbation theory," *PoS* **LATTICE2021** (2022) 489, `arXiv:2111.14376 [hep-lat]`.

[27] H. Takaura, R. V. Harlander, and F. Lange, "Determining the quark mass with the gradient flow," *PoS* **LATTICE2024** (2025) 288, `arXiv:2411.13782 [hep-lat]`.

[28] H. Makino and H. Suzuki, "Lattice energy–momentum tensor from the Yang–Mills gradient flow—inclusion of fermion fields," *PTEP* **2014** (2014) 063B02, `arXiv:1403.4772 [hep-lat]`. [Erratum: PTEP 2015, 079202 (2015)].

[29] R. V. Harlander, Y. Kluth, and F. Lange, "The two-loop energy–momentum tensor within the gradient-flow formalism," *Eur. Phys. J. C* **78** no. 11, (2018) 944, `arXiv:1808.09837 [hep-lat]`. [Erratum: Eur.Phys.J.C 79, 858 (2019)].

[30] R. V. Harlander and T. Neumann, "The perturbative QCD gradient flow to three loops," *JHEP* **06** (2016) 161, `arXiv:1606.03756 [hep-ph]`.

[31] K. G. Chetyrkin and M. Steinhauser, "The relation between the MS-bar and the on-shell quark mass at order alpha(s)**3," *Nucl. Phys. B* **573** (2000) 617–651, `arXiv:hep-ph/9911434`.

[32] K. Hieda and H. Suzuki, "Small flow-time representation of fermion bilinear operators," *Mod. Phys. Lett. A* **31** no. 38, (2016) 1650214, `arXiv:1606.04193 [hep-lat]`.

[33] P. Nogueira, "Automatic Feynman graph generation," *J. Comput. Phys.* **105** (1993) 279–289.

[34] P. Nogueira, "Abusing QGRAF," *Nucl. Instrum. Meth. A* **559** (2006) 220–223.

[35] M. Gerlach, F. Herren, and M. Lang, "tapir: A tool for topologies, amplitudes, partial fraction decomposition and input for reductions," *Comput. Phys. Commun.* **282** (2023) 108544, `arXiv:2201.05618 [hep-ph]`.

[36] R. Harlander, T. Seidensticker, and M. Steinhauser, "Corrections of $\mathcal{O}(\alpha\alpha_s)$ to the decay of the Z boson into bottom quarks," *Phys. Lett. B* **426** (1998) 125–132, `arXiv:hep-ph/9712228`.

[37] J. A. M. Vermaseren, "New features of FORM," `arXiv:math-ph/0010025`.

[38] J. Kuipers, T. Ueda, J. A. M. Vermaseren, and J. Vollinga, "FORM version 4.0" *Comput. Phys. Commun.* **184** (2013) 1453–1467, `arXiv:1203.6543 [cs.SC]`.

[39] K. G. Chetyrkin and F. V. Tkachov, "Integration by parts: The algorithm to calculate β-functions in 4 loops," *Nucl. Phys. B* **192** (1981) 159–204.

[40] P. Maierhöfer, J. Usovitsch, and P. Uwer, "Kira—A Feynman integral reduction program," *Comput. Phys. Commun.* **230** (2018) 99–112, `arXiv:1705.05610 [hep-ph]`.

[41] P. Maierhöfer and J. Usovitsch, "Kira 1.2 Release Notes," `arXiv:1812.01491 [hep-ph]`.

[42] J. Klappert and F. Lange, "Reconstructing rational functions with FireFly," *Comput. Phys. Commun.* **247** (2020) 106951, `arXiv:1904.00009 [cs.SC]`.

[43] J. Klappert, F. Lange, P. Maierhöfer, and J. Usovitsch, "Integral reduction with Kira 2.0 and finite field methods," *Comput. Phys. Commun.* **266** (2021) 108024, `arXiv:2008.06494 [hep-ph]`.

[44] R. V. Harlander, T. Nellopoulos, A. Olsson, and M. Wesle, "ftint: Calculating gradient-flow integrals with pySecDec," *Comput. Phys. Commun.* **306** (2025) 109384, `arXiv:2407.16529 [hep-ph]`.

[45] S. Borowka, G. Heinrich, S. Jahn, S. P. Jones, M. Kerner, J. Schlenk, and T. Zirke, "pySecDec: A toolbox for the numerical evaluation of multi-scale integrals," *Comput. Phys. Commun.* **222** (2018) 313–326, `arXiv:1703.09692 [hep-ph]`.

[46] K. G. Chetyrkin, J. H. Kühn, and M. Steinhauser, "RunDec: A Mathematica package for running and decoupling of the strong coupling and quark masses," *Comput. Phys. Commun.* **133** (2000) 43–65, `arXiv:hep-ph/0004189`.

[47] B. Schmidt and M. Steinhauser, "CRunDec: a C++ package for running and decoupling of the strong coupling and quark masses," *Comput. Phys. Commun.* **183** (2012) 1845–1848, `arXiv:1201.6149 [hep-ph]`.

[48] F. Herren and M. Steinhauser, "Version 3 of RunDec and CRunDec," *Comput. Phys. Commun.* **224** (2018) 333–345, `arXiv:1703.03751 [hep-ph]`.

[49] M. Lüscher, "Future applications of the Yang-Mills gradient flow in lattice QCD," *PoS* **LATTICE2013** (2014) 016, `arXiv:1308.5598 [hep-lat]`.

[50] M. Beneke and H. Takaura, "Gradient-flowed operator product expansion without IR renormalons," `arXiv:2510.12193 [hep-ph]`.